Available online at www.sciencedirect.com
SCIENCE DIRECT®
International Journal of Heat and Mass Transfer 49 (2006) 366–376
International Journal of HEAT and MASS TRANSFER
www.elsevier.com/locate/ijhmt

Direct simulation of falling droplet in a closed channel

Ming-Jiu Ni [a,*], Satoru Komori [b], Neil B. Morley [a]

[a] Department of Mechanical and Aerospace Engineering, University of California at Los Angeles, Los Angeles, CA 90095-1597, United States
[b] Department of Mechanical Engineering, Kyoto University, Kyoto 606-8501, Japan

Received 30 July 2004; received in revised form 25 March 2005
Available online 2 November 2005

Abstract

The direct simulation of a droplet falling in a different background liquid is presented. The complete Navier–Stokes problem is solved using a projection method coupled with a level set method. A detailed analysis is given to show that reinitialization procedure of level set method [M. Sussman, P. Smereka, S. Osher, Level set approach for computing solutions to incompressible two-phase flow, Journal of Computational Physics 114 (1) (1994) 146–159] cannot preserve the volume of a droplet. A variable time step method is presented to improve conservation. We study the effect of a wall on the droplet motion by settling a single circular droplet through a quiescent fluid at different lateral positions between parallel walls. The effect of inertial force on the deformation and oscillatory motion of a droplet is investigated by changing the Reynolds numbers. The deformation mechanism is studied for different Weber numbers. In addition, the interaction effect between droplets is studied by settling two and three droplets in the parallel channel. The Karman vortex distribution is shown to explain the oscillatory mechanism of droplet motion.

Keywords: Interfacial flows; Karman vortex; Deformation; Level set method

1. Introduction

The study of droplet deformation and breakup is of great importance to applications such as mixing in multiphase systems, blending of molten polymers, ink-jet printers, deformation of biological cells, atmospheric rain drop formation. Eggers [1] reviewed the theoretical development of non-linear dynamics and breakup of free-surface flows. Stone [2] summarized the capillary instability of droplet deformation and breakup in viscous flows at low Reynolds number. For the low Reynolds number flows, fluid motion is governed by the Stokes and continuity equations and the degree of droplet deformation and characteristics of breakup are largely determined by the magnitude of interfacial tension stresses relative to the magnitude of the flow-generated viscous stresses. The viscosity ratio and capillary number are two key dimensionless parameters for the low Reynolds number flows. For small Reynolds numbers, weak effects of inertia may be determined by perturbation of the Stokes solution. Leal [3] has noted that the cumulative effect of weak inertia can produce large effects that not predictable by linear theory. Explicit analytical solutions of fully non-linear problems of fluid-particle motions have rarely been obtained. Feng et al. [4] investigated the non-linear effects of fluid-particle motion by a finite

* Corresponding author. Tel.: +1 310 794 9198.
E-mail address: mingiiu@fusion.ucla.edu (M.-J. Ni).

0017-9310/$ - see front matter © 2005 Published by Elsevier Ltd.
doi:10.1016/j.ijheatmasstransfer.2005.03.025

element method. They stressed that the major difficulty concerning the non-linear effects appear when (a) the Reynolds number is large enough for inertia to be important, (b) the fluid is non-Newtonian and the flow is inherently non-linear and (c) the particle is deformable. In their study, only the case of the rigid particle in Newtonian fluids was considered without particle deformation. Mortazavi and Tryggvason [5] conducted the study of the motion of neutrally buoyant droplets in Poiseuille flow. Francois and Shyy [6,7] did the calculations of drop dynamics. The immersed boundary technique [6,8,9] is used to treat moving two-fluid boundaries. Mashayek et al. [10] studied the coalescence collision of two liquid drops using a Galerkin finite element method in conjunction with the spine-flux method for surface tracking.

The purpose of this study is to numerically clarify the effects of droplet deformation, breakup and inertia on fluid motion. The unsteady incompressible Navier–Stokes equations will be solved by a level set method. In Section 2, we analyze the reinitialization procedure for the level set method. A detailed analysis is given to show that the original reinitialization cannot conserve the mass. A variation time step method is presented to overcome the problem. In Section 3, we validate the computation method by calculating the broken dam problem [11] and bubble rising driven by buoyancy [12]. We then simulate the following flow situations in which droplet-fluid, inter-droplet and droplet-wall interaction, and deformation and breakup of droplets are fully manifested:

(i) The settling of a single circular droplet through quiescent fluid between parallel walls. We study the initial value problem in which a droplet begins falling from rest and we look at time-dependent solutions on the trajectories of the droplets. We will try to understand the effects of wall repulsion, inertia, and deformation on the droplet motion.
(ii) Interaction of two and three droplets in a channel. We will give special attention to the pattern of interactions among the droplets and walls.

The Karman vortex street is shown to explain the oscillation mechanisms of droplet falling flows in a channel.

2. Numerical algorithms

By employing a CSF (continuum surface force) model [13,14] of the surface tension force for the level set approach [15,16] the surface tension is reformulated as a volume force $\vec{F}_{SV} = k(\phi)\delta_\alpha(\phi)\nabla\phi$. The governing equations of an incompressible interfacial flow can be written as:

$$\frac{\partial u_i}{\partial x_i} = 0 \tag{1}$$

$$\frac{\partial u_i}{\partial t} + \frac{\partial}{\partial x_j}(u_i u_j) = -\frac{1}{\bar{\rho}}\frac{\partial p}{\partial x_i} + \frac{1}{\bar{\rho} Re}\frac{\partial}{\partial x_j}\left(\bar{\mu}\left(\frac{\partial u_i}{\partial x_j} + \frac{\partial u_j}{\partial x_i}\right)\right) - \frac{g_i}{Fr} - \frac{k(\phi)\delta(\phi)\nabla\phi}{\bar{\rho} We} \tag{2}$$

with dimensionless groups of the Reynolds, Froude and Weber numbers as $Re = \rho_1 LU/\mu_1$, $Fr = U^2/gL$, and $We = \rho_1 LU^2/\sigma$ respectively. $\bar{\mu}(=\mu/\mu_1), \bar{\rho}(=\rho/\rho_1)$ are the dimensionless ratios of the viscosity and density. For simplicity, hereafter we denote $\bar{\mu}$ and $\bar{\rho}$ as μ and ρ respectively. To prevent numerical instability, it is necessary to smooth the values of the density ρ and viscosity μ as:

$$\rho_\varepsilon(\phi) = \lambda_\rho + (1-\lambda_\rho)H_\varepsilon(\phi) \tag{3}$$

$$\mu_\varepsilon(\phi) = \lambda_\mu + (1-\lambda_\mu)H_\varepsilon(\phi) \tag{4}$$

where $\lambda_\rho = \rho_2/\rho_1$, $\lambda_\mu = \mu_2/\mu_1$. ϕ is a smooth level set function, which is positive outside the interface, negative inside the interface and zero at the interface. $H_\varepsilon(\phi)$ is a Heaviside function, $\delta_\varepsilon(\phi) = \partial H_\varepsilon(\phi)/\partial\phi$ is a surface tension delta function and $k(\phi) = \nabla\cdot(\nabla\phi/|\nabla\phi|)$ is the interface front curvature. The following equation will evolve the zero level of $\phi = 0$ exactly as the actual interface moves:

$$\frac{\partial\phi}{\partial t} + u_i\frac{\partial\phi}{\partial x_i} = 0 \tag{5}$$

The above equations are solved using a second-order variable-density projection method [17]. For large time computations, keeping the level set function as a distance function is advantageous to the computation of the surface tension forces. Also keeping ϕ as a distance function will ensure that the front has a finite thickness for all time, and that values for $\rho(\phi)$ will not be greatly distorted. Sussman et al. [16] presented a reinitialization equation which can be reformulated as:

$$\phi_\tau + \boldsymbol{w}\cdot\nabla\phi = \mathrm{sign}_\varepsilon(\phi_0) \tag{6}$$

$$\phi(\vec{x},0) = \phi_0(\vec{x}) \tag{7}$$

where $\boldsymbol{w} = \mathrm{sign}_\varepsilon(\phi_0)\nabla\phi/|\nabla\phi|, |\nabla\phi| = \sqrt{\phi_x^2+\phi_y^2+\phi_z^2}$, and $\mathrm{sign}_\varepsilon(\phi_0) = 2(H_\varepsilon(\phi_0) - 1/2)$ the sign function.

We know the total mass is conserved in time for an incompressible flow. Theoretically, the solution ϕ of Eqs. (6) and (7) will have the same sign and the same zero level set as ϕ_0, which means the interface will not move as time progressing for the solution of Eqs. (6) and (7). Away from the interface ϕ will converge to $|\nabla\phi| = 1$. Therefore it will converge to the actual distance. The unmoved interface with $|\nabla\phi| = 1$ will ensure the total mass and volume conservation. However, the numerical discretization of the reinitialization equation of the level set function will not preserve the property

in general. In fact, the half-discretized form of Eq. (6) can be written as

$$\phi^{n+1} = \phi^n + \Delta\tau_0 \operatorname{sign}_\varepsilon(\phi_0)(1 - |\nabla\phi^n|) \tag{8}$$

For the case of $|\nabla\phi| > 1$ near the interface, we find from Eq. (8) that a big time step cannot ensure the discretized value of the level set function has the same sign as the initial value. That means the large time step cannot conserve the volume near the interface for the case of $|\nabla\phi| > 1$.

Consider the case of $\phi_0 > 0$, $\operatorname{sign}_\varepsilon(\phi_0) = 1$, and suppose the reinitialization process (8) can preserve the volume conservative, we should have $\phi^n > 0$. Then from Eq. (8), we have:

$$\phi^{n+1} = \phi^n + \Delta\tau_0(1 - |\nabla\phi^n|) \tag{9}$$

If $|\nabla\phi^n| \leqslant 1$, we have $\phi^{n+1} \geqslant \phi^n > 0$ and the interface does not move. However, if $|\nabla\phi^n| > 1$, we have $\phi^{n+1} = \phi^n - \Delta\tau_0(|\nabla\phi^n| - 1)$, which will be less than 0 when $\Delta\tau_0 > \phi^n/(|\nabla\phi^n| - 1)$ and the interface moves and the volume is not conserved. Similarly, for the case of $\phi_0 < 0$, $\operatorname{sign}_\varepsilon(\phi_0) = -1$, when $|\nabla\phi^n| > 1$ and $\Delta\tau_0 > -\phi^n/(|\nabla\phi^n| - 1)$, then $\phi^{n+1} > 0$ and the interface may be removed. In general, when $|\nabla\phi^n| > 1$ and $\Delta\tau_0 > |\phi^n/(|\nabla\phi^n| - 1)|$, the interface will be most possible to remove and the volume will not be conserved. We need to stress that near the interface, both ϕ_0 and ϕ^n are small values and $|\phi^n/(|\nabla\phi^n| - 1)|$ is a small value too, so the situation $\Delta\tau_0 > |\phi^n/(|\nabla\phi^n| - 1)|$ is very possible to happen for the points near the interface, the interface moves and the volume is not conserved. Also we cannot employ a very small constant of $\Delta\tau$ for the sake of saving computational time.

To overcome this difficulty, the variable time-step size method can be presented to conduct the solution of Eqs. (6) and (7). We have the following two methods to get the variable time step; the first one is based on the above analysis and we get the variable time step as:

$$\begin{cases} \Delta\tau = \min\left(\Delta\tau_0, \dfrac{\phi^n/\operatorname{sign}(\phi_0)}{|\nabla\phi^n| - 1}\right) \\ \quad \text{if } \operatorname{sign}(\phi_0) \neq 0 \text{ and } |\nabla\phi^n| > 1 \\ \Delta\tau = \Delta\tau_0 \quad \text{otherwise} \end{cases} \tag{10}$$

And the second way to get the variable time step is based on the criterion to preserve the total volume of interface. As stressed in [18], we conserve the volume of the domain by requiring that

$$\partial_t \int_\Omega H(\phi) = 0 \tag{11}$$

Then, we have the variable time step method, which is designed with time step as:

$$\begin{cases} \Delta\tau = \Delta\tau_0(1 - \Delta\tau_0') \\ \quad \text{if } \operatorname{sign}(\phi_0) \neq 0 \text{ and } |\nabla\phi^n| > 1 \\ \Delta\tau = \Delta\tau_0 \quad \text{otherwise} \end{cases} \tag{12}$$

with

$$\Delta\tau_0' = \frac{\delta(\phi)(1+a)(1+a^2)(1+a^4)\int_{\Omega_{ijk}} \delta(\phi)\operatorname{sign}(\phi_0)a}{\operatorname{sign}(\phi_0)a\int_{\Omega_{ijk}}[\delta(\phi)]^2(1+a)(1+a^2)(1+a^4)} \tag{13}$$

Here $a = |\nabla\phi| - 1$. To accelerate the convergence, a two-stage Runge–Kutta technique with a larger time-step size can be taken in solving the re-initialization equation. The re-initialization procedure can be stopped when the relative error between the total mass at the current time and the initial mass is less than 10^{-6}. According to our computation, the average mass error using the variable time-step size method (12) and (13) was much less than that using the original re-initialization technique with the constant time-step size. However by employing the variable time step of (10) it is still possible that the interface will move half or one cell size since a positive level set function may be reduced to 0 and the minus level set function maybe enlarged to zero for the case of $|\nabla\phi^n| > 1$. So we prefer to use the variable time step formula (12) and (13), which can ensure the total volume conservative. According to our computation, the variable time-step size technique can get the same good results as the technique developed in [18].

About the mass conservation of level set method, it is necessary to give a brief introduction of CLSVOF method [19] and particle level set method [20]. CLSVOF method is a coupling method of VOF (volume-of-fluid) and level set method, in which volume fraction is used to reconstruct the interface to keep mass conservation while the level set function is used to calculate the curvature rate and surface tension. This method owns both of the advantages of VOF, which can keep mass conservation, and level set, which can accurately calculate the surface tension and normal direction of interface. However CLSVOF method also owns the disadvantages of VOF method: the interface needs to be reconstructed. This greatly limits the application of CLSVOF method for complicated geometry. Particle level set method is a coupling method of Lagrangian method and Eulerian method, which merges the best aspects of Eulerian front-capturing schemes and Lagrangian front-tracking methods for improved mass conservation in a fluid flow. Massless marker particles were inserted to correct mass loss in level set function by using the characteristic information of the escaped massless marker. This method maintains the nice geometric properties of level set method along with the ease and simplicity of implementation. The particle level set method compares favorably with volume of fluid methods in the conservation of mass and purely Lagrangian schemes for interface resolution.

However this method may cost more computational time compared with level set method and even CLSVOF method. For phase change with mass transfer across interface, there exist problems in setting up the massless marker particles for this particle level set method [21].

3. Simulation of drop falling flows

The dam break problem is calculated to further validate the method employed in this paper. A 81×41 uniform Cartesian grid is used with an initial water column height to width ratio of 2. $\rho_{water}/\rho_{back} = 1000$, $\mu_{water}/\mu_{back} = 1000$, and $Re = 1000$. At the outlet boundary, the Neumann boundary condition is set for velocities. At all other boundaries, slip wall boundary conditions are applied for the velocities. The variable time step method developed in Section 2 is employed to discretize the reinitialization equation. Fig. 1a illustrates the free surface profiles between time = 0.2 and time = 3.0 with time interval 0.2. The water surface evolves in a smooth shape and no oscillation occurs at the interface near the solid wall. Fig. 1b illustrates the mass loss using variable time step method. We can see that the total mass loss using variable time step method is less than 0.3%, while the original reinitialization procedure [16] can lose mass up to a total 1.75%. Fig. 2a shows the history of the water front marching along the ground surface ($y = 0$) and Fig. 2b shows the transient height of the wetted wall along the vertical surface ($x = 0$). Also the error bar in Fig. 2a shows the interface height in this calculation. The experimental results [11] are also shown in Fig. 2. The numerical results match the experimental data well. We also applied the developed method and code for the

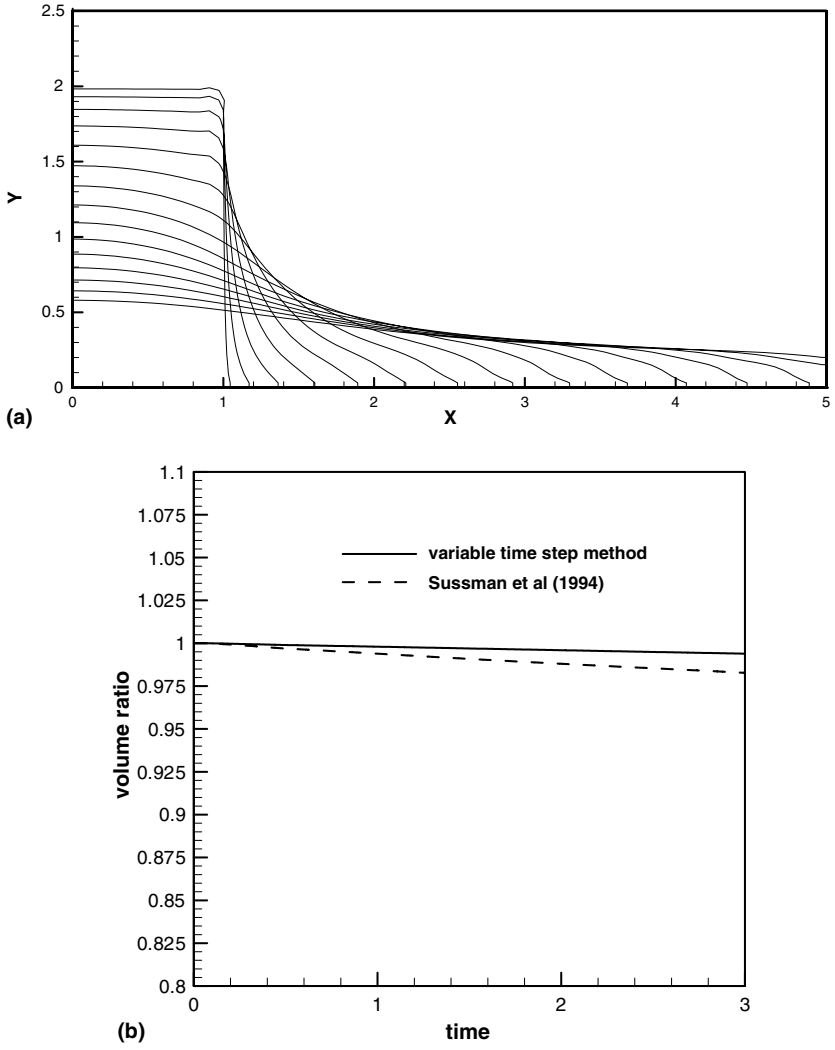

Fig. 1. (a) Zero level set contour from time = 0.2 to time = 3.0 with time interval 0.2 and (b) mass conservation history.

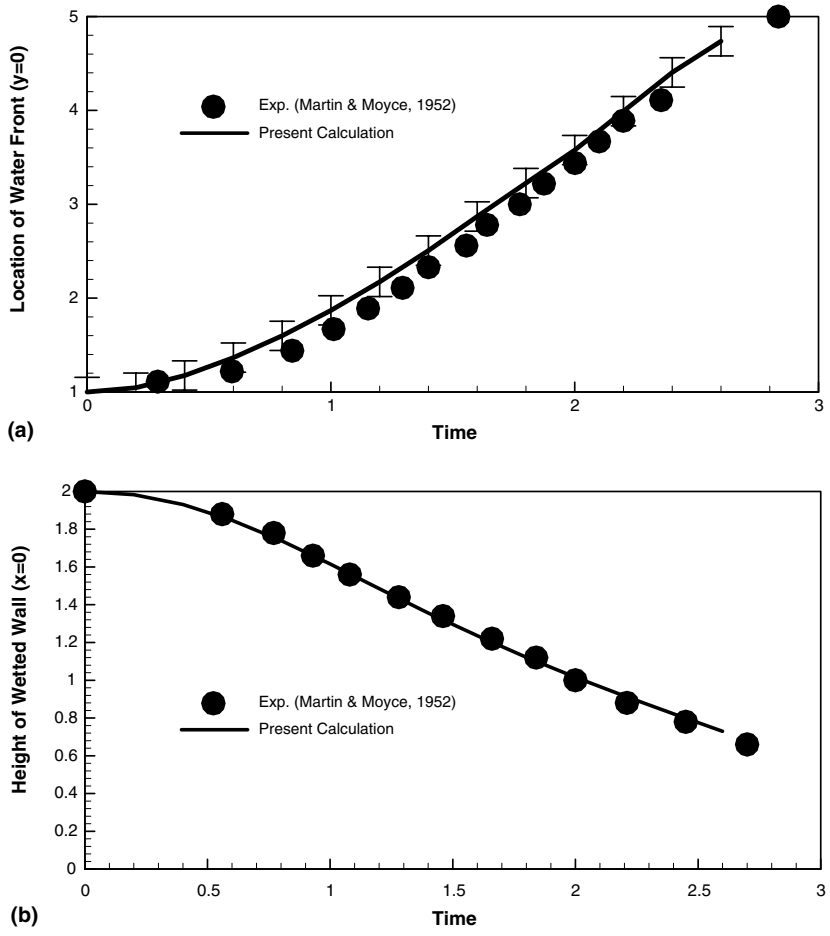

Fig. 2. History of water front location on solid surfaces in the dam break. (a) Location of water front at $y = 0$ and (b) height of wetted wall at $x = 0$.

simulation of 3D bubble rising in a channel, for which there exists experimental data. Fig. 3 shows the shapes from experiment [12], and from the computation conducted in this paper. They are very consistent, especially the curvature. This numerical test further validates the accuracy of the droplet falling calculation, which can be used to illustrate the deformation mechanisms and motion trajectory.

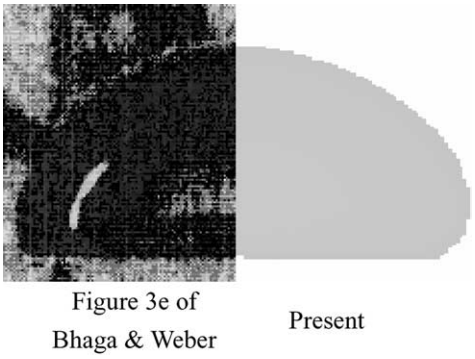

Fig. 3. Comparison of rising bubble shape with experiment at $Re = 13.4$, $We = 29$.

3.1. Droplet falling—to study mechanisms of motion and deformation

Feng et al. [4] studied the particle-fluid motion. According to their conclusions, a circular particle settling in vertical channel experiences different regimes at different Reynolds numbers, which is related to wake structure behind the particle. For the small Reynolds numbers, the particle drifts monotonically or with damping oscillations to a steady equilibrium on the centerline of the channel independent of the initial position of the particle. At a critical Reynolds number, the steady motion bifurcates into a oscillatory motion. When the Reynolds number is larger than the critical Reynolds

number, the periodic motion is unstable and gives way to irregular motion.

However, in Feng et al. study, the deformation of particles or droplets is not considered. We know deformation has a large effect on the motion, according to research results for low Reynolds number flow [22]. Since the computing the equilibrium position for the droplet flow with deformation is expensive, here we focus on the initial development of a droplet falling, considering the effects of the droplet deformation, wall repulsion and inertial force on the motion.

An initially stationary circular droplet of diameter $2R_0$ was released from different lateral positions in a rectangular channel with the width $9R_0$ and depth $18R_0$. The droplet was heavier than the fluid and started to move down, driven by gravity. Defining the characteristic velocity and length as $U = (gR_0)^{1/2}$ and $L = R_0$ respectively, we have dimensionless groups of Reynolds, Froude and Weber numbers as $Re = \rho_1 g^{\frac{1}{2}} R_0^{\frac{3}{2}}/\mu_1$, $Fr = 1$, and $We = \rho_1 g R_0^2/\sigma$. The free-surface boundary condition ($u = 0$, $\partial v/\partial y = 0$) was applied on the top and non-slip velocity conditions were applied on other walls with the initial condition $u_i(\tau = 0) = 0$. 97×193 collocated uniform meshes are employed for the computation. A four-level multigrid technique was employed for the solution of the pressure Poisson equation to enforce the divergence-free velocity. For this computation, the maximum residue of the velocity divergence in every computational cell was kept below 10^{-6}.

The shape development of a droplet falling in a liquid with a density ratio of $\lambda_\rho = \rho_g/\rho_l = 1.125$ is shown as a set of superimposed calculations in Fig. 4b. Fig. 4 illustrates that the droplet begins to fall down owing to gravity force. The color contours show the pressure distribution with high pressure as red and low pressure as blue. The pressure difference between the upper and lower surfaces forms the vortex chain at the corner of the upper surface, which induces the jet motion that pushes water into the droplet from above. Due to the effect of the jet, a velocity difference between the upper and lower surfaces is formed, and so the upper surface approaches the lower surface of the droplet. Due to the higher pressure difference between the upper and lower surfaces, which drives the lower surface up, the droplet flattens as time progressing. Eventually when the droplet is close to the bottom wall, the lower surface pierces into the top flat surface and the droplet is broken.

3.1.1. Effect of the wall on the motion

By settling droplets on different lateral positions in an initially quiescent fluid, the computational trajectories and velocity vectors results show the effects of the wall on the motion as shown in Fig. 4. Due to the wall shear, the droplet near the wall deforms and rotates (Fig. 4a). Due to wall repulsion, the deformed droplet moves to the centerline. When the droplet approaches the centerline, the pressure difference and the rotation force on the droplet will push the droplet back to the wall. When the droplet is close to the wall, the wall repulsion and the rotation force will drive the droplet to the centerline. The cycle is repeated and the droplet with initial lateral position near the wall has an oscillatory trajectory with increasing amplitude as time progressing due to the

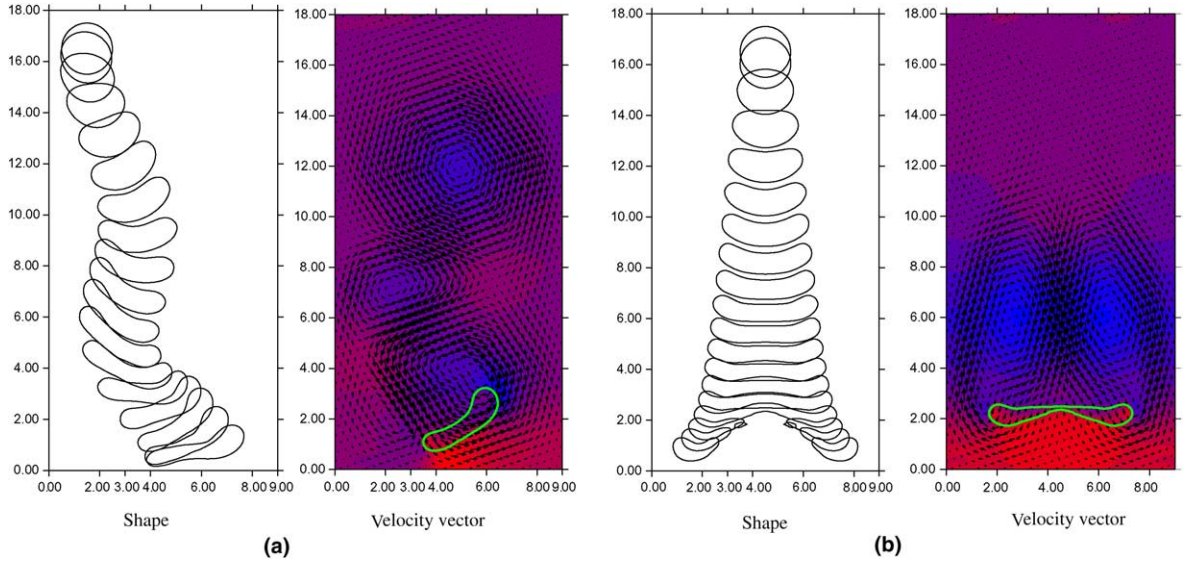

Fig. 4. Effect of wall on a falling droplet for $Re = 100$, $We = 50$, $\lambda_\rho = 1.125$, $\lambda_\mu = 50$. Droplet falling (a) near the wall with initial position (1.5, 16.5) and (b) in the central region with initial position at (4.5, 16.5).

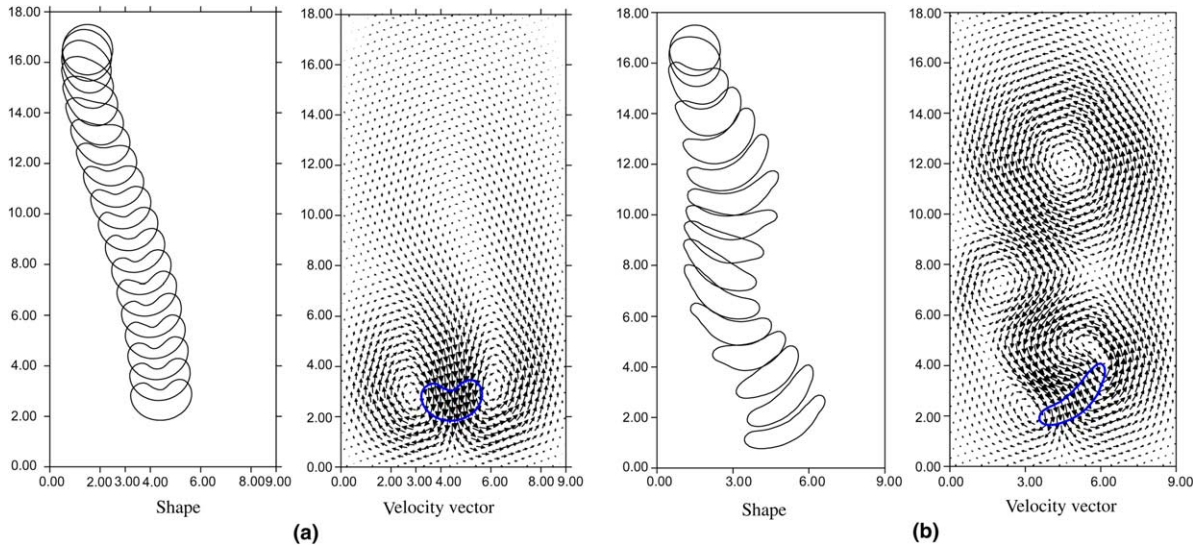

Fig. 5. Effect of viscous force on a falling droplet for $We = 50$, $\lambda_\rho = 1.125$, $\lambda_\mu = 5.0$ with initial position at (1.5, 16.5). (a) $Re = 10$ and (b) $Re = 100$.

increasing inertia. While the droplet with initial lateral position on the centerline, which is shown in Fig. 4b, falls straight along the centerline with no lateral motion since the Reynolds number or the inertia is not big enough to produce appreciable oscillation as found [4]. A vortex sheet is observed in the velocity vector of Fig. 4a for the falling movement of the droplet near wall, while only a vortex chain can be found in the velocity vector of Fig. 4b for the droplet movement along the centerline.

3.1.2. Effect of non-linear and viscous force on the deformation and motion

To study the effect of inertia on the motion, we settled two droplets near the wall with Reynolds numbers 10 and 100 respectively. For the low Reynolds number case of $Re = 10$ (Fig. 5a), the droplet initially moves to the centerline due to the wall repulsion; however, we cannot see the oscillatory trajectory due to the strong viscous damping. Eventually the deformed droplet falls down along a straight line near the centerline. For the case of $Re = 100$ (Fig. 5b), due to the large inertia, the droplet oscillates between the wall and the centerline. These oscillatory mechanisms have been described in the above subsection. The velocity vectors in Fig. 5a and b illustrate the effect of the inertia. The two vortices are generated symmetrically on the both sides of the deformed droplet for the low Reynolds number case of $Re = 10$ (Fig. 5a), while the non-symmetrical Karman vortex sheet illustrates the oscillatory mechanisms for high Reynolds number (Fig. 5b). Also for the low Reynolds number case of $Re = 10$, due to the strong viscous damping, the deformation of the droplet (Fig. 5a) is weak since the jet induced by the pressure difference between the top and bottom surfaces is weak. The droplet deformation for the large Reynolds number case of $Re = 100$ (Fig. 5b) is comparatively much larger.

3.1.3. Effect of surface tension on deformation and motion

Fig. 6 shows the trajectories and shapes for a falling droplet against the Weber numbers of 50 and 500. One droplet was settled down with initial lateral position on the centerline, while the other was settled down with initial position near walls. The droplet on the centerline will move down straight along the centerline as shown in Fig. 6b. The deformation for the droplet with $We = 500$ is larger than that for $We = 50$. The droplet near the wall oscillates due to the wall repulsion and inertia as shown in Fig. 6a. However, it is also shown that a larger deformation results in a larger oscillatory amplitude.

Fig. 7 shows the computational results for the small Weber number cases of $We = 5$ and 50 with initial lateral positions near the wall. For the case of $We = 5$ in Fig. 7a, the deformation is very small due to the large surface tension. Although we can see in Fig. 7a that the droplet is oscillating, the amplitude is very small, while the oscillatory amplitude in Fig. 7b is very strong for the larger deformed droplet for the case of $We = 50$. The velocity vectors also show that a larger deformation causes a stronger vortex and bigger oscillatory amplitude.

3.1.4. Effect of density ratio on the deformation and motion

Since the droplet falling is driven by the gravity, the density ratio will play a great role on the droplet motion

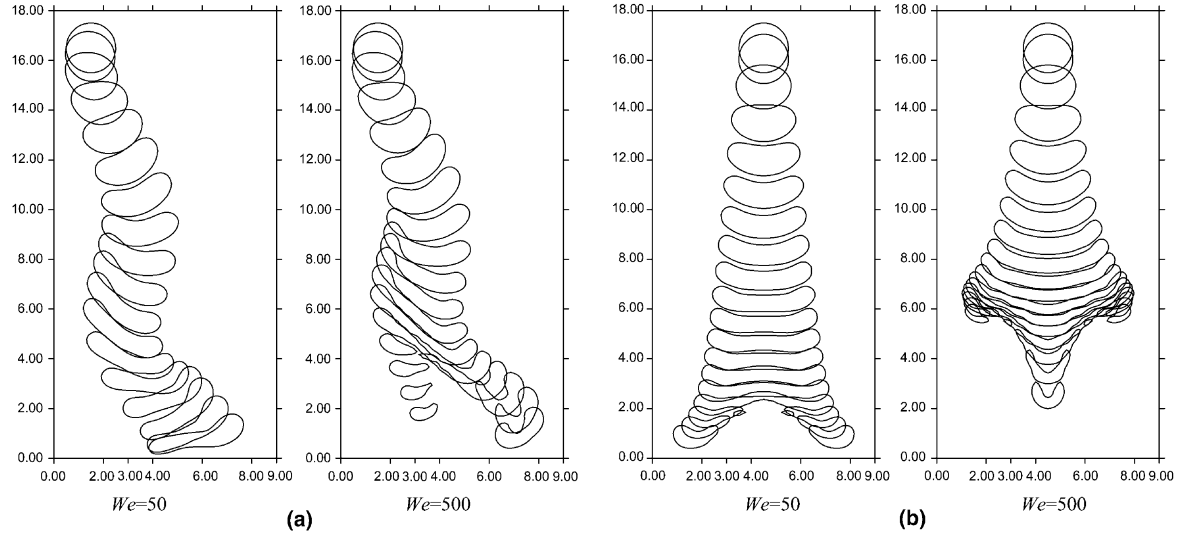

Fig. 6. Effect of surface tension on a falling droplet for $Re = 100$, $\lambda_\rho = 1.125$ and $\lambda_\mu = 50$. Droplet falling (a) near the wall with initial position (1.5, 16.5) and (b) in the central region with initial position at (4.5, 16.5).

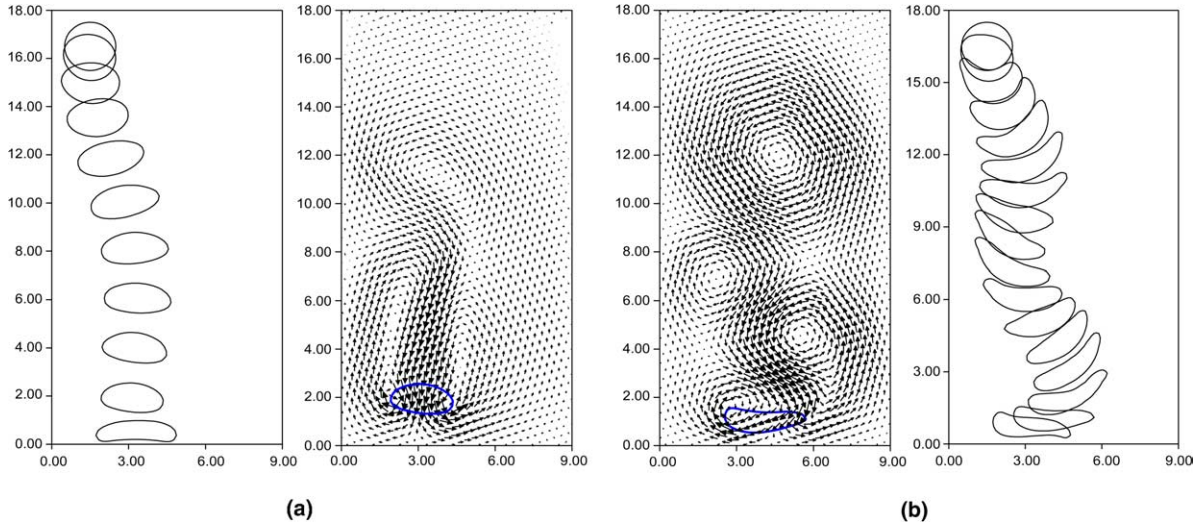

Fig. 7. Effect of surface tension on a falling droplet for $Re = 100$, $\lambda_\rho = 1.125$ and $\lambda_\mu = 1.0125$ with initial position at (1.5, 16.5). (a) and (b) $We = 50$.

in a liquid. Fig. 8 illustrates the effect of the density ratio on the trajectory and shape of the droplet. From the computation results, we can see that the deformation for the high density ratio of $\lambda_\rho = 1.125$ is larger than that for the case of low density ratio of $\lambda_\rho = 1.05$. For the higher density ratio, the Bond number is higher and the driven force is larger than that for the lower density ratio. The larger driven force will induce a stronger jet above the top surface of the droplet, which will produce larger deformation for the higher density ratio. Also, the falling speed of the droplet with high-density ratio is larger than the droplet with low density ratio. The inertial effect on the droplet motion of the high density ratio is stronger.

For the droplets near the wall as shown in Fig. 8a, the oscillatory amplitude for $\lambda_\rho = 1.05$ is smaller than for $\lambda_\rho = 1.125$ since the deformation and inertia for the case of low density ratio is weaker. The effects of deformation and inertia have been discussed in the above subsections.

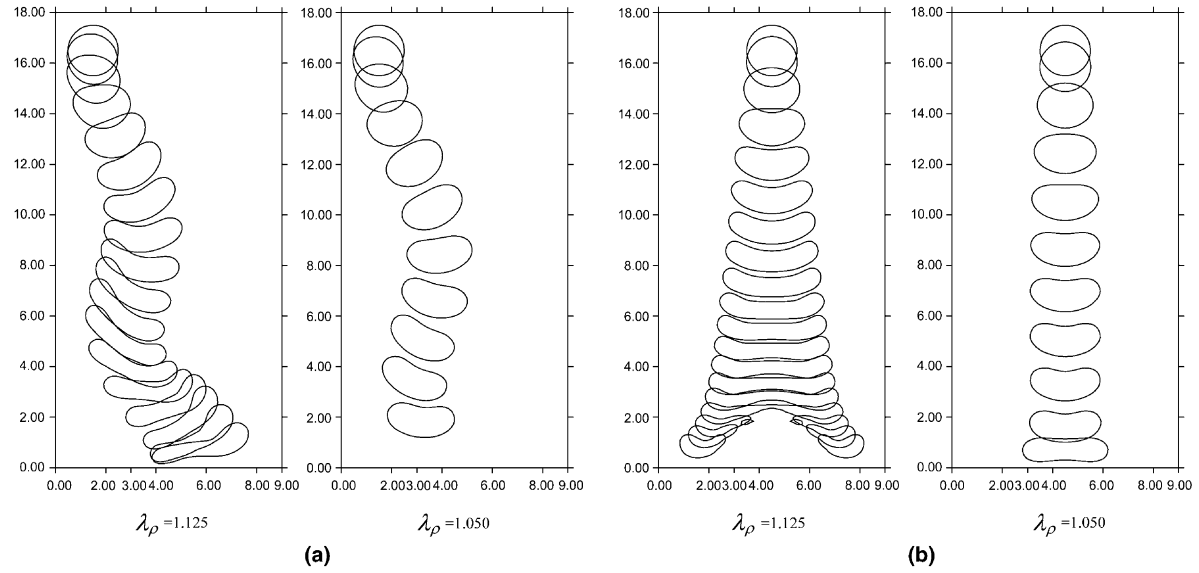

Fig. 8. Effect of density ratio on a falling droplet for $Re = 100$, $We = 50$, and $\lambda_\mu = 50$. Droplet falling (a) near the wall with initial position (1.5, 16.5) and (b) in the central region with initial position at (4.5, 16.5).

3.1.5. Effect of inter-droplet repulsion on multiple droplets

Fig. 9 illustrates the effect of the inter-droplet repulsion by settling two droplets symmetrically in the computational regions with same initial horizontal position. Fig. 9a and b show that the walls tend to push the two droplets together, while their mutual repulsion keeps them apart. Due to the large deformation and high inertia (since the Reynolds number and Weber number are relatively large), the two droplets exhibit oscillatory motion. It is expected that the two droplets move down along a steady straight line apart from the centerline when the Reynolds number is small enough.

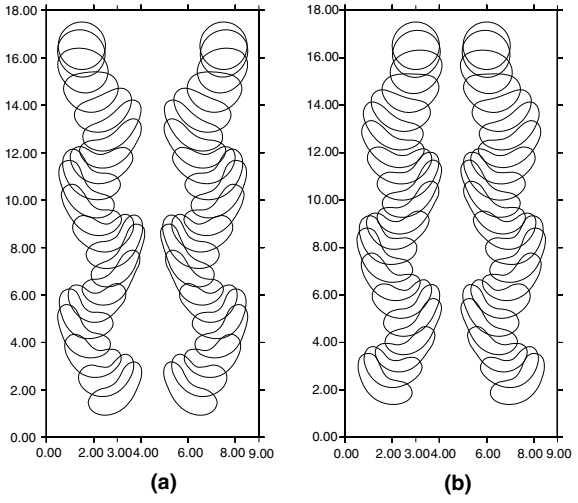

Fig. 9. Falling two-droplet flows for $Re = 100$, $We = 50$, $\lambda_\rho = 1.125$ and $\lambda_\mu = 50$. Droplet falling (a) near the wall with initial positions (1.5, 16.5) and (7.5, 16.5), (b) in the central region with initial positions at (4.5, 16.5), (3.0, 16.5) and (6.0, 16.5).

Fig. 10 illustrates the effect of inter-droplet and wall repulsion by settling three droplets from the same initial horizontal line. For the low viscosity ratio (Fig. 10a), due to the lower internal viscous damping force in the droplet, the deformation is large and eventually the three droplets coalesce into one big droplet. The new big droplet will continue to move down and exhibit even larger deformation since the Weber number has increased by $\sqrt{3}$ times over that of the original small droplet.

For the lower Weber number case with a big viscosity ratio (Fig. 10b), the deformation is smaller than in the smaller viscosity ratio case (Fig. 10a). Fig. 10b and c also illustrate the effect of surface tension on the deformation and motion of the droplets in a fluid. For the larger Weber number $We = 50$ (Fig. 10c), due to the lower surface tension, the droplets are greatly deformed. Finally, the central one is broken up into two droplets. The two droplets fall down with effects of wall repulsion and inter-droplet repulsion. Due to the smaller area and diameter of the new droplets, they deform less than the original larger one. Also due to the repulsion of the bottom wall, the two small droplets coalesce into the other two bigger droplets.

3.1.6. Coalescence of two droplets

For the two droplets settling in the same horizontal line, we cannot find the process of two droplets coalescing (see Fig. 9a and b). However when the droplets are ini-

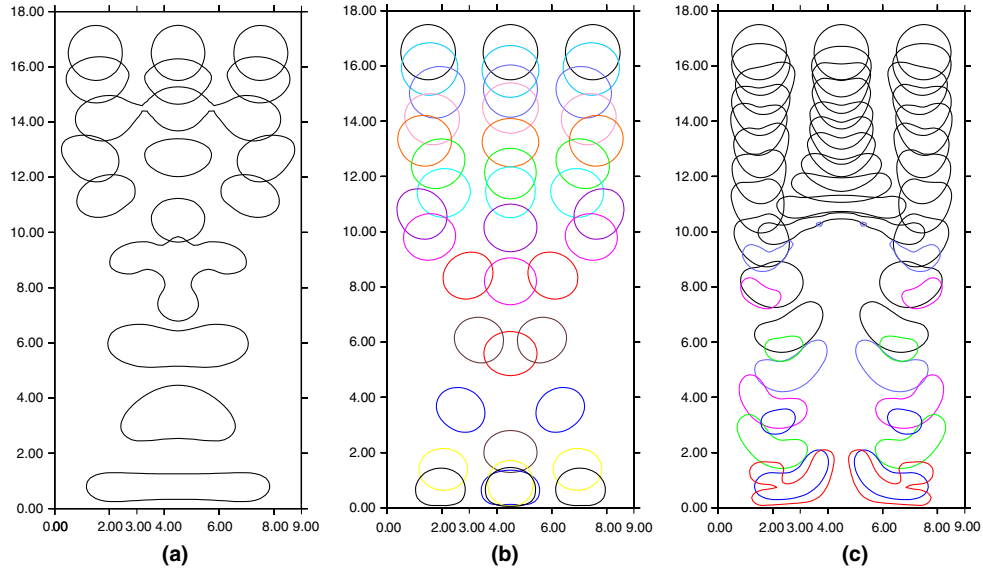

Fig. 10. Falling three-droplet flows for $Re = 100$ and $\lambda_\rho = 1.125$. (a) $We = 5$ and $\lambda_\mu = 1.05$. (b) $We = 5$ and $\lambda_\mu = 50$. (c) $We = 50$ and $\lambda_\mu = 50$.

tially settled at the centerline with one droplet above a second one as shown in Fig. 11, the trailing droplet accelerates into the wake of the leading droplet (Fig. 11b) and finally merges with it into a new droplet (Fig. 11c). The new droplet has a larger size than the old one (with Weber number $\sqrt{2}$ times large as the old one), and it deforms more than the old one due to the reduced effect of surface tension and viscosity (Fig. 11d). Fig. 11 illustrates this processing of the deformation, coalescence and larger deformation. The effects of Reynolds number, internal circulation, drop size ratio and impact velocity on the coalescence process has been investigated in detail by Mashayek et al. [10]. They also measured the period of oscillations for the combined drop and found that the first oscillation period is always shorter than the second period regardless of Reynolds number.

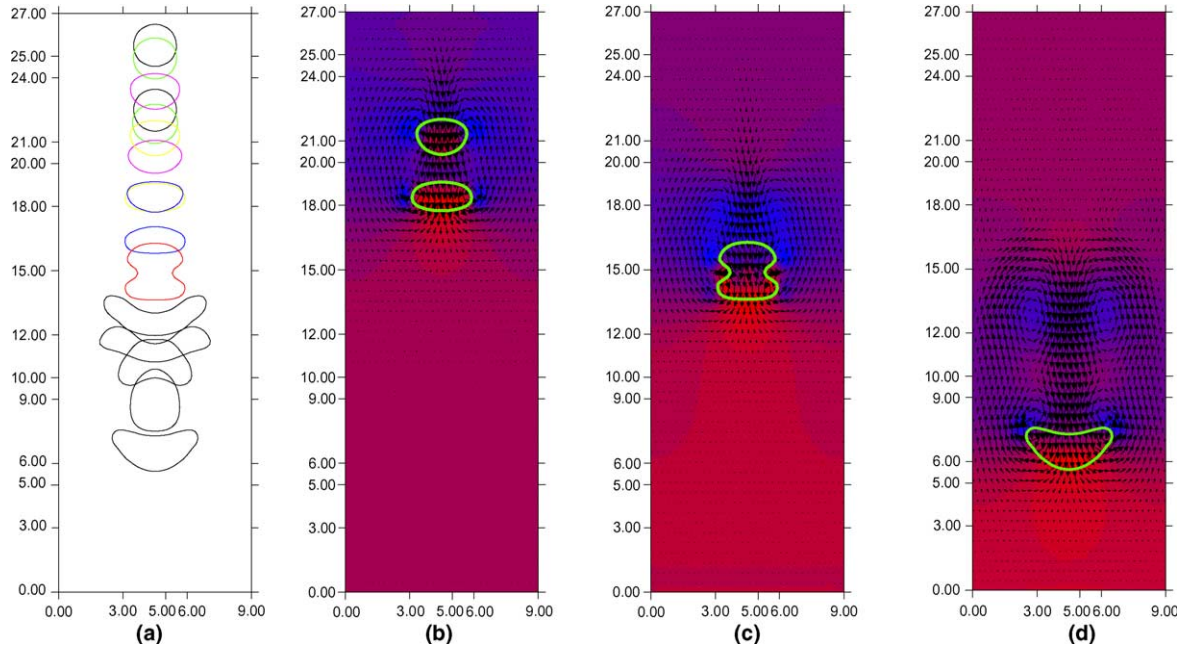

Fig. 11. Falling two-droplet flows for $Re = 100$, $We = 5$, $\lambda_\rho = 1.125$ and $\lambda_\mu = 1.0125$ with initial positions at (4.5, 25.5) and (4.5, 22.5).

4. Conclusion

The main results on the effects of wall repulsion, inter-droplet repulsion, inertia, and deformation on the motions of falling droplets can be summarized as follows:

(1) The Karman vortex street shown in the computation can explain the oscillatory mechanisms of the falling droplet motion in a lighter fluid. Due to the wall shear, the droplet near the wall deforms and moves towards the centerline of the channel. When the inertia is strong, the pressure difference and rotation force push a droplet near the centerline back to the wall, and the wall repulsion and the rotation force push the droplet near the wall to the centerline again. The cycle is repeated if the viscous damping is not large, and we can see the oscillatory trajectory. Larger deformation generates larger oscillatory amplitude. The connection between Karman vortex and inertia, droplet deformation and wall repulsion is shown.
(2) For two or three droplets initially settled symmetrically at the same horizontal location, the competition between wall repulsion and inter-droplet repulsion decides the direction of the droplet movement to the wall or to the centerline. The walls tend to push the droplets together and their mutual repulsion keeps them apart. When droplets are settled initially at the centerline with one droplet above another one, the leading one forms a low-pressure region after the droplet, which will accelerate the trailing one. The trailing one with a higher velocity finally coalesces with the leading one to form a larger droplet.

This paper also gives an analysis that the reinitialization method [16] can lose the total mass during the reinitialization procedure. A variable time step method is presented to improve the mass conservation of the level set method.

Acknowledgements

The authors would like to acknowledge the financial support by the JSPS (Japan Society for the Promotion of Science) through grant-in-aid (no. 14102016).

References

[1] J. Eggers, Nonlinear dynamics and breakup of free-surface flows, Rev. Modern Phys. 69 (3) (1997) 865–929.
[2] H.A. Stone, Dynamics of droplet deformation and breakup in viscous fluids, Ann. Rev. Fluid Mech. 26 (1994) 65–102.
[3] L.G. Leal, Particle motion in a viscous fluid, Ann. Rev. Fluid Mech. 12 (1980) 435–476.
[4] J. Feng, H.H. Hu, D.D. Joseph, Direct simulation of initial value problems for the motion of solid bodies in a Newtonian fluid. Part 1: Sedimentation, J. Fluid Mech. 261 (1994) 95–134.
[5] S. Mortazavi, G. Tryggvason, A numerical study of the motion of droplets in Poiseuille flow. Part 1: Lateral migration of one droplet, J. Fluid Mech. 411 (2000) 325–350.
[6] M. Francois, W. Shyy, Computations of drop dynamics with the immersed boundary method. Part 1: Numerical algorithm and buoyancy-induced effect, Numer. Heat Transfer B 44 (2) (2003) 101–118.
[7] M. Francois, W. Shyy, Computations of drop dynamics with the immersed boundary method. Part 1: Numerical algorithm and buoyancy-induced effect, Numer. Heat Transfer B 44 (2) (2003) 119–143.
[8] C.S. Peskin, Numerical analysis of blood flow in the heart, J. Comput. Phys. 25 (3) (1977) 220–252.
[9] S.O. Unverdi, G. Tryggvason, A front tracking method for viscous, incompressible, multifluid flows, J. Comput. Phys. 100 (1) (1992) 25–37.
[10] F. Mashayek, N. Ashgriz, W.J. Minkowycz, B. Shotorban, Coalescence collision of liquid drops, Int. J. Heat Mass Transfer 46 (1) (2003) 77–89.
[11] J.C. Martin, W.J. Moyce, An experimental study of the collapse of liquid columns on a rigid horizontal plane, Philos. Trans. Roy. Soc. Lond. Ser. A—Math. Phys. Sci. 244 (882) (1952) 312–324.
[12] D. Bhaga, M.E. Weber, Bubbles in viscous liquids: Shapes, wakes and velocities, J. Fluid Mech. 105 (1981) 61–85.
[13] J.U. Brackbill, D.B. Kothe, C. Zemach, A continuum method for modeling surface tension, J. Comput. Phys. 100 (2) (1992) 335–354.
[14] Y.C. Chang, T.Y. Hou, B. Merriman, S. Osher, A level set formulation of Eulerian interface capturing methods for incompressible fluid flows, J. Comput. Phys. 124 (2) (1996) 449–464.
[15] S. Osher, J.A. Sethin, Fronts propagating with curvature-dependent speed: Algorithms based on Hamilton–Jacobi formulations, J. Comput. Phys. 79 (1) (1988) 12–49.
[16] M. Sussman, P. Smereka, S. Osher, A level set approach for computing solutions to incompressible two-phase flow, J. Comput. Phys. 114 (1) (1994) 146–159.
[17] M.-J. Ni, M. Abdou, S. Komori, A variable density projection method for interfacial flows, Numer. Heat Transfer B 44 (6) (2003) 553–574.
[18] M. Sussman, E. Fatemi, An efficient, interface preserving level set re-distancing algorithm and its application to interfacial incompressible flow, SIAM J. Sci. Comput. 20 (4) (1999) 1165–1191.
[19] M. Sussman, E.G. Puckett, A coupled level set and volume-of-fluid method for computing 3D and axisymmetric incompressible two-phase flows, J. Comput. Phys. 162 (2) (2000) 301–337.
[20] D. Enright, R. Fedkiw, J. Ferziger, I. Mitchell, A hybrid particle level set method for improved interface capturing, J. Comput. Phys. 183 (1) (2002) 83–116.
[21] D. Enright, Private communication.
[22] H.A. Stone, L.G. Leal, The influence of initial deformation on the droplet breakup in subcritical time-dependent flows at low Reynolds numbers, J. Fluid Mech. 206 (1989) 223–263.